Helium spin-echo spectroscopy: studying surface dynamics with ultra-high-energy resolution

TOPICAL REVIEW

Helium spin-echo spectroscopy: studying surface dynamics with ultra-high-energy resolution

G Alexandrowicz and A P Jardine

The Cavendish Laboratory, JJ Thomson Avenue, Cambridge CB3 0HE, UK

E-mail: ga232@cam.ac.uk

Abstract
Spin-echo measurements offer a major step forward in the technique of helium atom surface scattering. The experimental energy transfer resolution has been improved by several orders of magnitude, and has resulted in an expansion in the range of surface systems which can be studied. We describe the measurements within a double Fourier transform formalism, which by using appropriately selected 'tilted projections' for measurement allows elastic, inelastic and quasi-elastic measurements to be treated on an equal footing. We illustrate the wide scope of application for helium spin-echo with measurements from each of these areas.

(Some figures in this article are in colour only in the electronic version)

Contents

1. Introduction

The dynamical behaviour of atoms and molecules at surfaces represents some of the most important and fundamental processes in surface physics and chemistry. The way an atom moves and vibrates on a surface reflects the underlying atomic-scale interactions and energy transfer mechanisms. Measuring the surface dynamics on the relevant lengthscale and timescale provides a unique opportunity to study these underlying processes [1].

Over the past 30 years, helium atom scattering (HAS) has proven a flexible and powerful experimental technique, allowing many surface-dynamical problems to be studied. Its scientific uptake was driven by two major technological advancements, namely the development of supersonic molecular beam sources [2, 3] and of high-speed detection techniques. These enabled the velocity distribution in a surface-scattered helium beam to be determined with high resolution, permitting a huge range of energy-resolved measurements of both substrate and adsorbate vibrational modes [4]. The application of the spin-echo technique to helium beams, which forms the topic of this review, provides another major leap in energy resolution and opens up a wide range of additional systems which can now be studied with a helium probe.

In the present paper, we review and illustrate both the principle and application of helium-3 spin-echo techniques to surface dynamics. We present a graphical description of the spin-echo measurement [5] which allows elastic, inelastic and quasi-elastic experiments to be treated equally. We then illustrate the major scientific benefits of ultra-high resolution through a range of experimental measurements covering each of these three regimes. Finally, we look towards what we believe will be an exciting future for the technique.

2. The motivation for helium-3 spin-echo

While many techniques exist for probing surfaces, the unique properties of thermal energy helium atom beams, namely inertness, low energies and a de Broglie wavelength comparable to the atomic spacing in matter mean they have found wide application in both structural and dynamical problems [4, 6]. Time-of-flight methods have been used to measure the velocities in the scattered helium beam and hence study surface dynamics through energy transfer relations. The ultimate energy resolution of such measurements, which is typically ∼0.3 meV, is dictated by the monochromaticity of a helium beam. Inelastic and quasi-elastic measurements obtained in this way are actually the convolution of the instrumental resolution and real physical process being examined. While the technique has provided decades' worth of remarkable measurements on a multitude of surface modes, the energy resolution represents a significant limitation for many systems. For example, quasi-elastic scattering measurements, which rely on measuring a diffusion-induced broadening of the otherwise elastically scattered beam, have been limited to a handful of systems which move exceptionally quickly [7, 8]. An improved resolution means that such measurements can be improved in two distinct ways. First, the technique can be extended to a wider range of previously unaccessible 'slow-moving' systems (in section 4.3.2 measurements which are well outside the previously accessible time range are described). Second, higher resolution means it becomes possible to determine the true lineshape of quasi-elastic processes, rather than having to assume a particular dependence (the usefulness of this ability is illustrated in section 4.3.3). However, the need for resolution is not limited to quasi-elastic measurements. A lack of sufficient resolution means vibrational modes of heavy adsorbates or weakly coupled systems cannot be identified, while studying the lineshape and anharmonicity of vibrational modes is restricted.

The energy resolution limit is addressed using a novel technique known as 'spin-echo'. The technique was first applied to neutron beams by Mezei [9], and it allows measurements

to be made with orders of magnitude higher energy resolution, since it circumvents the spread of energies in the incident beam. Only changes in the energy which occur on scattering are measured, by using the nuclear spin of each individual beam particle as an independent internal clock. The technique is explained in the following section using the 'wavelength matrix' description [5].

The spin-echo technique was first applied to helium beams by the Heidelberg group [10], where a 33 neV change in the beam energy was detected, using extremely low-energy helium beams. While these low-energy beams allow unique studies of long-range gas–surface interactions [11], they also limit the application of the technique in surface science, where significant momentum transfers are also important. For example, in quasi-elastic measurements large momentum transfers are necessary to probe short length scales, enabling the dynamics to be studied on an atomic scale.

In the last few years, hexapole magnets which polarize and focus much higher energy and intensity helium beams have been successfully developed [12, 13]. Consequently, the design of the Cambridge ^{3}He spin-echo spectrometer was optimized in order to address both resolution and momentum-transfer issues [14]. The resolution and momentum-transfer requirements conflict, since a higher momentum beam passes through the precession fields more quickly, reducing the effective resolution. A compromise was drawn, using a 8 meV beam energy and achieving a nominal energy resolution of 3 μeV at this energy. A nominal 45° total scattering geometry was used to make effective use of the momentum in the incident helium beam, allowing measurements up to about 4 Å^{-1}.

Finally, it is worth pointing out that the spin-echo technique does not replace the time-of-flight method. In both helium and neutron scattering, spin-echo provides higher resolution, but is much less appropriate for measuring large energy changes. As such the two techniques are complementary.

3. The two-dimensional wavelength intensity matrix model of spin-echo

The equations describing the signal measured in a spin-echo experiment can be derived analytically using either classical [9] or quantum mechanical [15] derivations. In this paper, we will start by presenting an alternative graphical description for helium spin-echo [5], which starts with the classical approach to describe the spin dynamics, and relates the measured beam polarization to the incoming and scattered de Broglie wavelength of the helium atoms. This description of the spin-echo experiment provides a general framework within which we can simultaneously describe the application of the technique to elastic, inelastic and quasi-elastic scattering experiments. Finally, when describing surface diffusion measurements, the complementary time-domain description of the experiment will be discussed. The time-domain description of the experiment facilitates interpretation of the surface-diffusion mechanism from the experimental data.

We will start by following the spin dynamics through the main components of the helium spin-echo apparatus, shown schematically in figure 1, the details of which have been published in more detail elsewhere [14]. The ^{3}He beam, produced in the source, is first passed through a polarizer stage. This consists of a hexapole magnetic field [12] followed by a dipole magnetic field, and plays a two-fold role. The polarizer splits the two polarization components of the beam and dumps one into the vacuum system. The other is transmitted, forming the fully polarized beam. In addition, the polarized beam is also focused into a parallel beam of ≈2 mm diameter, aimed at the sample, avoiding the $1/R^2$ intensity loss of a diverging beam. Here, we define the spin orientation of the polarized beam as the Y axis.
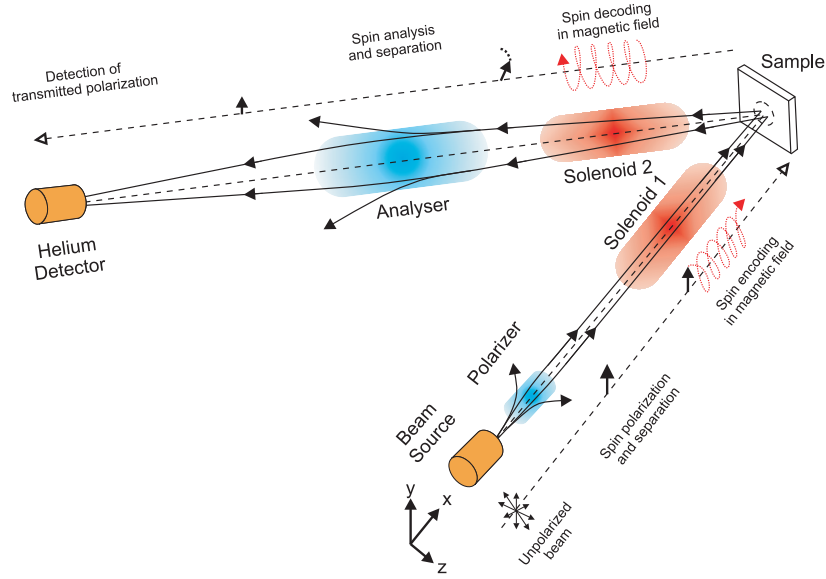
Figure 1. A schematic view of the ^{3}He spin-echo spectrometer. The beam, produced at the source, is spin polarized and focused into a parallel beam by the polarizer stage. At the end of the polarizer the spin orientation of the beam is aligned along the 'Y' axis. The beam enters the first precession field, which is a magnetic field oriented along the 'X' axis produced by a solenoid coil. Within this magnetic field, the spins undergo Larmor precession and are encoded with a spin phase related to their de Broglie wavelength. After scattering from the sample the atoms pass through a second solenoid field which encodes a second spin phase related to the scattered wavelength. Finally, the atoms pass through a spin analyser which transmits (and focuses) the beam into the particle detector. The transmission probability into the detector is proportional to the projection of the spin phase on the positive 'Y' axis. In the quantum picture, described in section 4.3.1, the precession fields are treated as interference elements which separate and recombine two wavepackets in time and space.

The polarized ^{3}He beam then enters the first precession field. This magnetic field is aligned along the beam direction (X axis), and is produced by driving a current through a solenoid coil enclosing the beam line. The nuclear spin of the atoms entering this field is aligned perpendicular to the field direction. Thus, like in an NMR experiment, the nuclear spins will precess in the plane perpendicular to the field direction (the YZ plane), with a frequency given by the Larmor relation, $\omega_L = \gamma B$, where γ is the gyromagnetic ratio of ^{3}He and B is the magnitude of the magnetic field. Within the magnetic field region the atoms accumulate a spin phase. For a constant field this will simply be the product of the angular frequency and the time spent in the field, or in terms of the atom velocity, V, the phase is simply $\phi = \omega_L x / V$, where x is the length of the magnetic field region. It is useful at this stage to express the accumulated phase using the de Broglie wavelength, λ,

$$\phi = 2\pi \kappa \lambda, \qquad \kappa \equiv \frac{1}{2\pi h} \gamma m B_{\mathrm{eff}} I \qquad (1)$$

where we define an experimentally controllable parameter, κ, which is proportional to the current we apply. The B_{eff} term is the path integral of the precession field, per unit current, and m is the mass of ^{3}He.

After passing through the first precession field, the atoms enter the ultra-high vacuum (UHV) scattering chamber and scatter from the surface of the sample[1]. The scattered atoms

---

[1] An additional 'spin rotator field' [5] is located in between the two solenoids inside the scattering chamber. This field rotates the spin phase by 45° around the 'Y' axis, compensating for the fixed scattering geometry of the apparatus.

then enter a second precession field created by a solenoid coil which is identical to the first coil. Again, during the flight through the magnetic field the atoms accumulate a spin phase given by equation (1). The total spin phase is simply the sum of the two independent phases, i.e. $\phi = 2\pi(\kappa_1\lambda_1 + \kappa_2\lambda_2)$, where the subscripts denote the different values of current used in the two fields and the possible difference between the incident and scattered wavelengths.

Finally, the beam enters the spin analyser [13] which acts as a magnetic filter stage before entering the particle detector, located at the end of the beam line. Like the polarizer, the spin analyser is a combination of hexapole and dipole magnetic fields, which focus one spin component into the detector and dump the other into the vacuum system. This combination of magnetic fields gives us a count rate at the detector which, after subtracting a constant term, is simply proportional to the beam polarization measured with respect to the Y axis.

3.1. The two-dimensional wavelength intensity matrix

Using equation (1) to calculate the spin phase, the polarization can be written as

$$P_Y(\kappa_1, \kappa_2) \propto \int \int_{\lambda_{\min}}^{\lambda_{\max}} I(\lambda_1, \lambda_2)[\cos(2\pi(\kappa_1\lambda_1 + \kappa_2\lambda_2))] \, d\lambda_1 \, d\lambda_2 \qquad (2)$$

where the integration is performed over all the different wavelengths existing in the incoming and scattered beams. We define the wavelength intensity matrix, $I(\lambda_1, \lambda_2)$, as the relative probability of detecting an atom, at a given scattering geometry, which had a wavelength of λ_1 before scattering and a wavelength λ_2 after scattering. Within some simplifying assumptions[2], the value of the wavelength intensity matrix at a certain λ_1, λ_2 coordinate can be also expressed as the product of two probability functions $I(\lambda_1, \lambda_2) \propto \rho(\lambda_1)S(\lambda_1 \rightarrow \lambda_2)$. $\rho(\lambda_1)$ denotes the wavelength distribution function within the incident beam, while the scattering probability function, $S(\lambda_1 \rightarrow \lambda_2)$, is defined as the probability of an event where the helium atom, which is scattered by the surface into the geometry of the experiment, changes wavelength from λ_1 to λ_2.

Equation (2) defines a two-dimensional (2D) cosine Fourier transform relation between the measured polarization and the wavelength intensity matrix. Thus, measuring the polarization over a sufficient range of κ_1, κ_2 (I_1, I_2) values should allow us to reconstruct the wavelength intensity matrix defined above. In order to appreciate the physics contained in the wavelength intensity matrix, we will start by describing the events in a typical helium-scattering experiment. A surface is never perfectly flat on the lengths corresponding to typical helium wavelengths. Hence, even when the scattering geometry does not correspond to a Bragg reflection condition, a certain portion of the beam will always be scattered elastically, e.g. from defects. However, if the scattering centres which reflect the helium beam are not static then the scattering process will not be perfectly elastic [16, 17]. In particular, when the surface motion is aperiodic, then the scattered beam energy (and wavelength) distribution will be broader than the corresponding distribution in the incident beam. This process is called quasi-elastic scattering and will be discussed in more detail in a later section (section 4.3). In addition to the elastic or quasi-elastic scattering, a certain portion of the beam will excite/de-excite surface phonons. As a result, a fraction of the beam will undergo a net loss/gain of energy and will be scattered inelastically from the surface.

Figure 2 illustrates a wavelength intensity matrix, $I(\lambda_1, \lambda_2)$, which corresponds to this simplified scattering experiment. The matrix is zero everywhere except for three high-intensity features. The central linear feature corresponds to elastic or quasi-elastic scattering. The

---

[2] For simplicity, the wavelength dependence of the transfer probability through the magnetic lenses and the ionization probability at the atom detector are neglected.
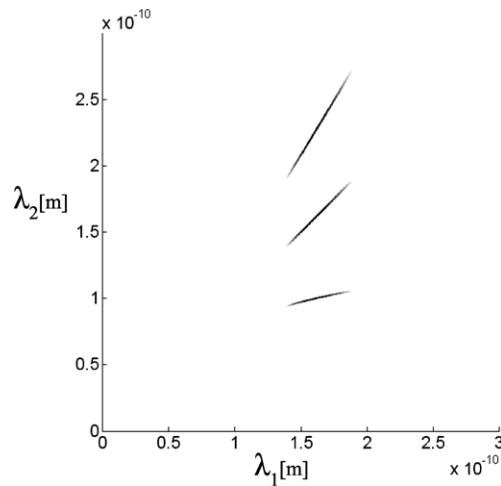
Figure 2. Illustration of the wavelength intensity matrix. The three linear features are regions where the matrix has non-zero values. The central line is due to elastic (or quasi-elastic) scattering whereas the lines above and below arise from energy loss and energy gain processes, e.g. surface phonon creation and annihilation.

location of this line, along the 45° diagonal, reflects the elastic condition, $\lambda_1 = \lambda_2$. The position and horizontal spread of this feature (parallel to the λ_1 axis) are dictated by the position and width of the incident beam wavelength distribution function, $\rho(\lambda_1)$. The much smaller width of the line reflects the range of different λ_2 values allowed for a specific λ_1 value. For example, if the scattering is perfectly elastic it will be a delta function, whereas if the surface is dynamic then the scattering probability function, $S(\lambda_1 \rightarrow \lambda_2)$, will no longer be a delta function. In this case, the width of the quasi-elastic feature in the wavelength intensity matrix is a direct measurement of the motion taking place on the surface.

The two additional features above and below the elastic line arise from energy-loss and energy-gain processes due to the creation and annihilation of surface phonons. The vertical displacement between these features and the elastic feature corresponds to the absolute value of energy loss/gain (wavelength gain/loss) reflecting the dispersion curve of the inelastic process studied. In a similar way to the elastic case, the distribution of the wavelengths in the incident beam governs the horizontal position and spread of these features. The much smaller width of these features reflects the linewidth and corresponding lifetime of the inelastic excitation. This important physical property reflects the rate at which the vibrating species can exchange energy with it surroundings.

In time-of-flight helium-scattering experiments, the elementary restriction on energy resolution arises from the finite width of the energy distribution within the incident beam. The fact that the width of the quasi-elastic and inelastic features within the wavelength intensity matrix can be measured in a way which is independent of the incident beam distribution makes the prospect of reconstructing this 2D matrix very appealing. Unfortunately, such reconstruction requires extensive 2D scanning of the κ_1, κ_2 space. Given the current sensitivity of the particle detector, this process takes too long to be practical in UHV studies of reactive surface systems. However, as will be shown below, the 'Fourier projection theorem' allows us to retain the attractive features of the wavelength intensity matrix measurement mentioned above, using a more 'economic' 1D measurement.
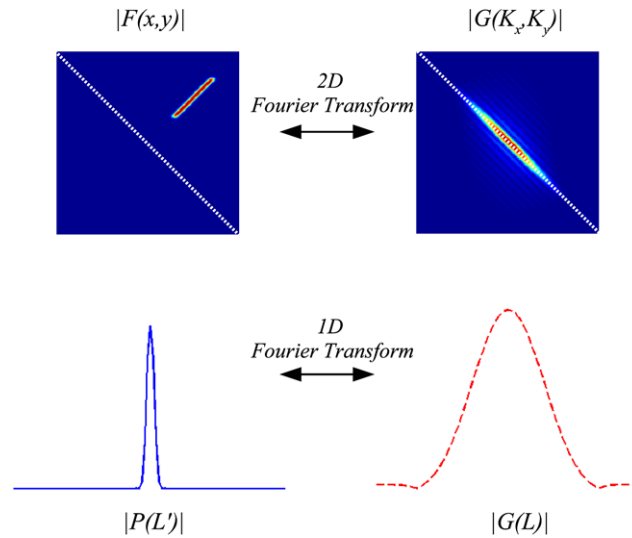
Figure 3. The two upper panels show two 2D matrices, related by a 2D Fourier transform. In general, these matrices contain both real and imaginary values. For simplicity, only the amplitudes are plotted in the figure. The lower right panel shows the amplitude of $G(L)$, a 1D measurement of $G(K_x, K_y)$ along the diagonal line L marked by the dashed white line. The amplitude of the Fourier transform of $G(L)$ is plotted on the lower left panel. The projection theorem states that this vector is identical to the result obtained by projecting $F(x, y)$ onto the diagonal axis marked with the dashed white line in the upper left panel.

3.2. Tilted projection measurements

The Fourier projection theorem, a simple consequence of the definition of a Fourier transform, is illustrated in figure 3. The two upper panels in this figure show a pair of 2D matrices labelled $F(x, y)$ and $G(K_x, K_y)$, which are related through a 2D Fourier transform. Next we measure the values of $G(K_x, K_y)$ along a certain axis, L, shown by the dashed white line in the upper right panel, and call the resulting 1D vector $G(L)$. The amplitude of $G(L)$ is plotted in the lower right panel of the figure. The lower left panel shows the amplitude of the 1D Fourier transform of $G(L)$, which we label as $P(L')$. The projection theorem states that $|P(L')|$ is identical to the projection of $F(x, y)$ onto an axis in the (x, y) space which is parallel to the L axis. This projection axis is indicated by the dashed white line in the upper left panel. The consequence of this theorem is that we can reconstruct a projection of $F(x, y)$ along any axis we choose using a suitable 1D measurement of $G(K_x, K_y)$.

Figure 4 superimposes the wavelength intensity matrix, shown previously in figure 2, with different examples of 1D projections. The upper panel of figure 4 illustrates schematically two simple projections, a horizontal projection labelled 'A' and a vertical projection labelled 'B'. The horizontal projection is simply the sum over all the matrix rows. This projection is obtained by measuring the polarization while scanning the magnitude of the first precession field and maintaining the second field at zero (i.e. measuring $P(\kappa_1, \kappa_2 = 0)$) and then Fourier transforming the result. Since all the different λ_2 values are summed together, the resulting vector does not contain any direct information about the inelastic and quasi-elastic processes. For smooth surfaces, where the probability of scattering into a given geometry does not vary significantly as a function of the incoming energy (i.e. $\rho(\lambda_1) \int S(\lambda_1 \rightarrow \lambda_2) \, \mathrm{d}\lambda_2 \propto \rho(\lambda_1)$), the horizontal projection simply reproduces the wavelength distribution in the incident beam. Measuring a horizontal projection at specular scattering conditions, where the signal is strong
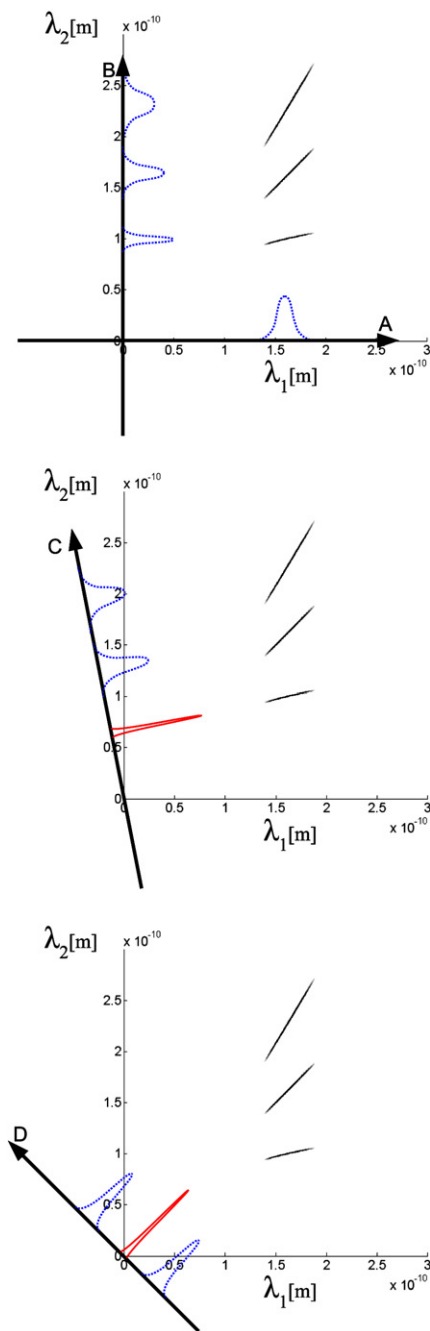
Figure 4. Illustration of the tilted projection measurement principle. The lines labelled 'A', 'B', 'C' and 'D' represent four different projection axes. The projection of the wavelength intensity matrix onto these axes is drawn schematically on top of the corresponding axes. Note that along the 'A' and 'B' axes, all the projected peaks are broadened by varying amounts, due to the finite width of the incident wavelength distribution. In contrast, the sharp peak in projection 'C', which is a projection of the energy gain (wavelength loss) feature, and the sharp peak in projection 'D', which corresponds to the elastic peak, maintain the true width of the inelastic process. The two peaks which are reconstructed from optimized projections are plotted using a full line.

and elastic scattering overwhelms the total signal, is standardly used to characterize the wavelength distribution of the beam.

A more interesting scenario is encountered when the horizontal projection is measured for corrugated surfaces. In this case, the scattering probability is a rapidly changing function of the incoming energy (wavelength) and the resulting spectrum will be characterized by various peaks and dips in the intensity. These features in the spectra correspond to selective adsorption resonances, and allow us to study the helium–surface interaction precisely. An example of such a study is given in section 4.1.

Next, we look at the second projection, labelled 'B', shown in the upper panel of figure 4. This vertical projection is obtained in a similar manner to projection 'A', but using only the second precession field (i.e. measuring $P(\kappa_1 = 0, \kappa_2)$). The three high-intensity lines are converted into three peaks in the projection spectrum. Measuring this vertical spectrum gives the same information obtained from a time-of-flight experiment. In the present example, the position of the elastic peak and the two inelastic peaks can be clearly seen in the projected spectrum. While the location of these peaks can be used to study the dispersion of energy gain/loss processes, the width and the exact location of the peaks are convoluted with the incident beam distribution, making it particularly difficult to measure subtle features such as quasi-elastic peak width, inelastic peak width and small anharmonicity shifts.

The projections labelled 'C' and 'D', which are shown in the middle and lower panels of figure 4, illustrate the solution to the convolution problem. If we utilize the fact that the high-intensity lines are predominantly linear, we can project the wavelength intensity matrix onto an axis which is oriented perpendicular to one of these high-intensity lines. When the measurement is performed at an optimally tilted projection, the projected peak we wish to study will retain the true width of the original 2D feature, independent from the wavelength distribution function of the incident beam. In addition, since all the different incident wavelengths will contribute to this sharp peak, the peak will retain a high signal to noise ratio, even if we use a beam with a broad distribution of wavelengths. The projection 'C', shown in the middle panel, was optimized for the energy-gain (wavelength-loss) peak, as illustrated by the narrow width of the projected peak. Projection 'D', shown in the lower panel, illustrates the optimal projection for measuring a quasi-elastic peak.

In order to measure the polarization matrix along a certain axis, the following procedure is performed: the polarization is measured while scanning the current vector magnitude, defined as $I = \sqrt{I_1^2 + I_2^2}$, between zero and the requested maximal value while keeping the ratio I_1/I_2 fixed. Defining the tilted projection angle, α, as the angle between the tilted axis and the positive horizontal axis, the condition for measuring a projection which is optimized to measure the width of a certain peak is simply $d\lambda_2/d\lambda_1 = -\tan(\alpha) = -I_1/I_2$, where $d\lambda_2/d\lambda_1$ is the gradient of the high-intensity feature we wish to project. For example, projection 'D', which is optimized for measuring the width of the elastic peak, is tilted by $\alpha = 135°$ with respect to the positive horizontal axis, equivalent to the conventional spin-echo condition, $I_1 = -I_2$.

The ability to tilt the projections discussed above allows us to perform an optimal 1D measurement of the wavelength intensity matrix. When using the optimal projection, a dramatic improvement in the wavelength resolution and the corresponding energy resolution of the reconstructed spectra is achieved. The actual resolution of the Cambridge apparatus and the various factors limiting the resolution are discussed in the appendix.

3.3. Double-phase spin-echo measurements

Equation (2) relates the measured polarization along the Y direction and the wavelength intensity matrix through a cosine Fourier transform. The symmetry property of a cosine

transform means that any reconstructed spectrum will always be symmetrical about its origin (i.e. the true features which appear on one side of the spectrum will also be mirrored onto the 'wrong side' of the spectrum). In some situations this artefact will be of no importance. For example, let us look at projections 'A' or 'B' in figure 4. Using a cosine transform, the reconstructed spectrum will also contain mirror image peaks, located at negative wavelength values. For clarity these peaks were not included in the figure. Since these artefact peaks are well separated from the true peaks and have no physical meaning (they correspond to a reversed beam direction!) they will not cause any confusion. However, when we measure a general tilted projection measurement, for example projection 'D' in figure 4, real features are expected at and on both sides of the origin, and it will be difficult to identify the real and the mirror peaks. In particular, real peaks which overlap with mirror peaks and asymmetrical peaks located at the origin will be severely distorted.

In order to avoid these artefact peaks the full Fourier transform of the wavelength intensity matrix needs to be measured. The ideal way of doing this is to repeat the measurement with a 90° angle between the direction in which the beam is polarized and the direction in which it is analysed. In this case, the expression for the polarization would be identical to that given in equation (2), with the exception that the cosine would be replaced by a sine function. Redefining the original measurement, P_Y as P_{real} and the 90° rotated measurement mentioned above as P_{imag}, we can define a complex polarization, $P = P_{real} + \sqrt{-1} P_{imag}$, which is a full Fourier transform of $I(\lambda_1, \lambda_2)$. Measuring the complex polarization in a tilted projection experiment allows us to reconstruct the projected spectrum fully without the artefacts mentioned above.

Currently, all the existing spin-echo instruments (neutron and helium) have a fixed angle between the analyser and polarizer magnetic field, making it difficult to measure P_{imag} directly. A different solution which was implemented at this stage is to measure P_{imag} by adding an additional 90° rotation in the first precession field. Since the strength of the field needed to rotate the magnetization in the precession coil depends on the atom velocity, this solution is accurate only for a perfectly monochromatic beam. However, since the total rotation needed is small and the procedure is performed before scattering, the deviations from an ideal Fourier transform are small and the mirror peaks described earlier are significantly reduced in size. An example of this procedure and its restrictions will be given in section 4.2.

4. Experimental application

4.1. Elastic scattering: selective adsorption resonance and helium–surface potentials

The helium-3 spin-echo technique is primarily aimed at achieving high-energy resolution for inelastic and quasi-elastic scattering. However, the unique nature of the technique also provides an unusual approach to measuring the rapid changes in reflectivity with incident helium energy that characterize selective adsorption resonances [18–21]. One of the main applications of selective adsorption measurements has been to enable the development of highly accurate helium–surface potentials. Such potentials are important for quantitative interpretation of helium-scattering experiments, and more recently have been highlighted as highly accurate tests of first-principles theory, particularly where dispersive forces are important.

4.1.1. Selective adsorption resonance. Selective adsorption of helium at surfaces was one of the earliest atom scattering phenomena to be observed [22], and was seen only shortly after the very first atom–surface diffraction experiments [23]. Since then, selective adsorption resonances (SARs) have been studied on a wide range of surfaces [6, 24]. The phenomenon is

a transient form of trapping at the surface. When an atom is scattered by a periodic surface, the kinematically allowed **G**-vectors for scattering correspond to scattering into 'open' channels, i.e. into real diffracted beams. It is also possible for a particle to be diffracted into a channel which is kinematically forbidden, providing it simultaneously occupies a bound state of the atom–surface potential, such that

$$E = \frac{\hbar^2 \mathbf{k}_i{}^2}{2m} = \frac{\hbar^2 (\mathbf{K}_i + \mathbf{G})^2}{2m} + E_n(\mathbf{K}_i, \mathbf{G}), \tag{3}$$

where, following the usual convention, we use upper-case type to denote 2D vectors in the surface plane. The process can take place only if the difference between the energy of the incident atom and the kinetic energy of the atom moving on the surface matches the binding energy of the adsorbed atom, E_n. It is this phenomenon which is termed a selective adsorption resonance or a bound state resonance. It is characterized by sharp changes in the reflectivity as the resonance condition is passed. Conventional experiments have typically involved measuring the specular helium reflectivity of a sample, while either the scattering geometry or the beam energy is varied. However, the angular resolution or the velocity spread in the beam, respectively, limit the quality of the measurements.

Since selective adsorption features correspond to the bound-state energies within the helium–surface potential, they provide a natural approach to determining the shape of the potential [24]. The atom–surface bound state energies are typically related to the data using a free atom model (FAM), where the atom is considered as free to move laterally over the surface, but is confined in the perpendicular direction. Here, the resonance energy is related directly to one of the bound states of the laterally averaged potential well. The approach is valid in the limit of low corrugation and has been used with considerable success, although, more generally, the binding energy would be expected to be a function both of the wavevector, **K**, and the diffraction vector **G** [25, 26]. Selective adsorption measurements are generally applicable and can be obtained for any helium–surface potential providing that (a) the surface is sufficiently corrugated to get good diffraction into the bound states and (b) the surface quality is sufficiently good that the resonance lifetime is long enough to give a narrow enough lineshape.

4.1.2. SAR measurements using helium-3 spin-echo. Rather than scanning the incident helium beam energy, the spin-echo instrument is used to measure simultaneously a complete distribution of scattered energies, in a process that is directly analogous to other forms of Fourier transform spectroscopy. The sample is flooded with a broad spread of helium energies. Assuming the scattering is predominantly elastic, we can then use an $\alpha = 0°$ or $90°$ projection measurement (i.e. using only either the incoming or outgoing coil), followed by Fourier transformation, to determine the spectrum of energies in the elastically scattered part of the beam. Since the intensity profile of the helium beam is well known and varies slowly with energy compared to selective adsorption features (and can also be measured directly by performing such a scan while scattering from a flat surface), we can determine the reflectivity variation due to selective adsorption.

An example of a selective adsorption measurement is illustrated schematically in figure 5. Figure 5(a) shows the polarized intensity that would be obtained with an $\alpha = 0°$ or $90°$ scan on a suitably corrugated surface, while (b) illustrates the corresponding Fourier transform. The overall envelope of the transformed result resembles the peak projected onto axis 'A' in figure 4 (i.e. the result on a smooth surface), with the important exception that the beam profile is now significantly modulated by a number of sharp selective adsorption features. The high-frequency oscillations in figure 5(a) correspond to the mean beam energy in (b), while the rapid initial decay at small currents corresponds to the broad spread of energies. The beat-like features in
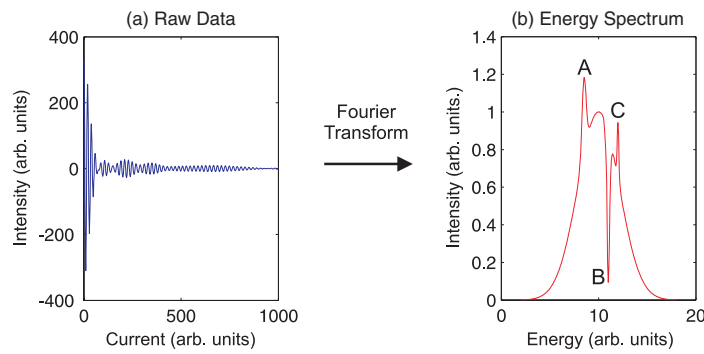
11

Figure 5. Illustration of a typical one-coil measurement (i.e. using an $\alpha = 0°$ or $90°$ projection) measurement that includes selective adsorption processes. (a) shows the polarized intensity obtained by ramping the current in one of the precession coils; (b) shows the beam energy profile obtained by Fourier transforming the raw measurement and converting to an energy scale. Features 'A'–'C' represent selective adsorption features.

(a) are due to the sharp changes in reflectivity labelled 'A'–'C', and correspond to the selective adsorption processes. The principal advantages of this approach is that a very high resolution is available to identify sharp resonances (along with their width) and simultaneous measurements are carried out on many features, meaning that large amounts of data can be acquired quickly.

The most comprehensive selective adsorption resonance data set which was obtained to date was for the LiF(100) surface [18, 19]. This data set was obtained for on-specular measurements using a $44.4°$ scattering geometry and energies between 4 and 16 meV. The azimuthal range was scanned between the two principal axes of the surface ($\langle 100 \rangle$ to $\langle 110 \rangle$), and for each azimuthal measurement, yielded a 1D spectrum as illustrated in figure 5(b). The complete data set is difficult to handle, but can be conveniently visualized by arranging the individual traces next to each other to form a 2D plot. The data set is shown this way in figure 6, using colour to represent the logarithm of the intensity (red is highest intensity and blue is lowest), as a function of both energy and azimuthal orientation of the sample [19]. The red band running through the centre of the plot corresponds to the broad peak in the energy spread of the incident beam. The high-intensity peaks and dips running through the data and dispersing with azimuth (such as the feature labelled 'A') are due to selective adsorption resonances. It is worth noting that plotting the data in this way makes several of the weaker features clearly visible; these are difficult to distinguish from the noise in any single azimuthal linescan.

Initial analysis of the data set was performed in terms of a free-atom model (FAM) [19]. The diffraction thresholds, the energies at which particular diffraction channels become available, are plotted in figure 6 as solid black lines. The bound states then exist at an interval below these lines, corresponding to the bound-state energy. The FAM fit to the observed features, shown as dashed blue lines in figure 6, gives 29 different values falling into four approximate energy levels that are consistent with earlier measurements. The position of each FAM line can be fitted considerably more accurately than the spread in the values around each of the four approximate energy levels. Similarly, a number of experimental features diverge from the FAM lines, such as the lines labelled B, which cross within the FAM but avoid each other within the data. The fact that different selective adsorption features for the same approximate energy level occupy slightly different energies, combined with the explicit deviation from the FAM seen in a few cases illustrates the limits of the model.

Recent calculations have dramatically improved upon the level of analysis usually presented in the literature [18, 19, 21]. The approach here was to use close coupled calculations
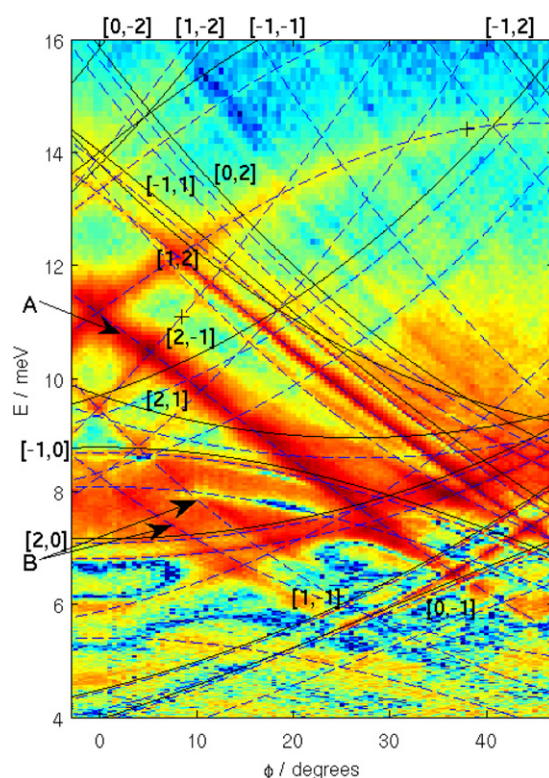
Figure 6. Complete on-specular selective adsorption resonance data set for ^{3}He–LiF(100) at 295 K, within a 44.4° total scattering geometry, using the incoming solenoid [19]. Intensity is represented by a log colour scale ranging from blue (lowest) to red (highest). Diffraction thresholds are shown by solid black lines (labelled with square brackets) and fitted free-atom model lines by dashed blue lines. 'A' and 'B' label features described in the text.

to compare the best existing potentials with the experimental data set directly, without the necessity for an intermediate model. Hence, the approach avoids previous difficulties of determining whether a particular selective adsorption process corresponds to a peak, dip or composite feature. The best existing potentials in the literature for this system are a semi-*ab initio* potential developed by Celli *et al* [27] in which an experimental C_6 term was incorporated, and a fully *ab initio* potential developed by Fowler–Hutson, then simplified by Eichenauer and Toennies [28, 29]. Both these pairwise potentials were compared with the new experimental data, revealing a number of small but systematic differences [19]. The width and depth of the potentials were scaled using both linear and nonlinear correction terms, in order to reproduce the experimental data. The resulting potential, which can be obtained by applying different scalings to either of the two starting potentials, is fully consistent with the measurements.

A similar quantity of data has also been obtained for the well ordered adsorbate system ^{3}He–c(2 × 2)CO/Cu(001) [20, 21]. In this case, the selective adsorption features were weaker and less well defined. The only existing potential for this system was constructed by Ellis *et al* [30], by adding an established He–Cu(001) potential to the gas phase He–CO potential, which was justified since CO–CO lateral interactions had been shown to be weak [31]. Comparing the selective adsorption data with calculations based on the existing potential shows that, this
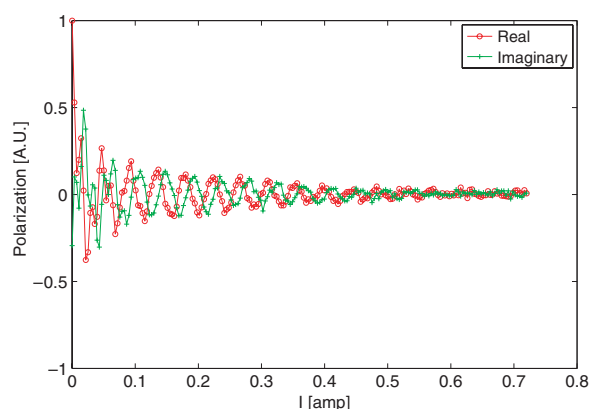
Figure 7. Real and imaginary polarization measured on a clean Cu(001) surface. The crystal was cleaned using 800 eV Ar+ sputtering and 800 K annealing cycles, and maintained in a UHV chamber with a background pressure of 1×10^{-10} mbar. The measurements were performed at 190 K, along the ⟨100⟩ crystal azimuth, $-5°$ off specular and with a tilted projection angle of $\alpha = 144°$.

time, theory is considerably less able to fit the data. The main discrepancy is that the potential clearly contains too many bound states, and they exist at incorrect energies. Although it was not possible to conclusively identify all the features in the data, by concentrating on the position and quantity of the strongest features, Riley *et al* [20, 21] were able to demonstrate that several alterations to the potential were necessary, and substantially improved the overall quality of the potential. These alterations included smoothing the shape of the laterally averaged potential and adjusting the depth of the well.

4.2. Inelastic scattering: measuring the anharmonicity of low-energy phonon modes

Time-of-flight helium atom scattering has been used extensively to study the low-energy surface phonons, both of clean surfaces and of adsorbate systems [4]. While the vibrational frequencies of many systems have been completely characterized, measurements of phonon line width and anharmonicity were restricted to a handful of systems where the experimental resolution did not hinder the measured quantities [32–34].

Figure 7 shows the real and imaginary polarization, measured as a function of the current vector magnitude ($\sqrt{I_1^2 + I_2^2}$) for a clean Cu(001) surface. The measurements were performed $-5°$ off the specular direction with a tilted projection angle $\alpha = 144°$ (where $\tan(\alpha) = I_1/I_2$). At small current values, the polarization fluctuates between the real and imaginary components in a complex fashion; however, at larger current values the polarization follows a well defined oscillatory pattern with a slowly decaying amplitude and a phase difference of ≈90° between the real and imaginary components. While the complex polarization curve seen at small currents promises multiple features in the reconstructed spectrum, the simple oscillation pattern seen at large currents indicates the existence of a single narrow peak which dominates the underlying spectrum.

Figure 8 shows the spectrum which was reconstructed from the polarization scan in figure 7. There are three main peaks in the spectrum, labelled 'E', 'R' and 'L'. The 'E' peak is the diffuse elastic peak. It is centered around the incident beam energy and corresponds to off-specular elastic scattering. The 'R' peak is an extremely narrow energy-loss peak which dominates the spectrum. It has a full width at half maximum of ≈70 μeV. The tilted projection
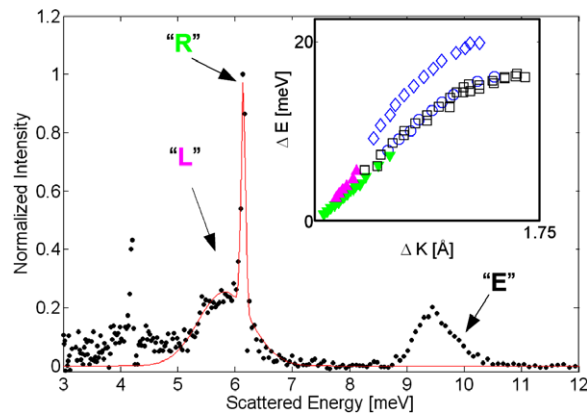
Figure 8. Energy spectrum reconstructed from the polarization scan shown in figure 7. The polarization was measured $-5°$ off specular. The three main features indicated as 'E', 'R' and 'L' are assigned to the diffuse elastic peak, the extremely narrow Rayleigh mode (FWHM $\approx 70\ \mu$eV) and the longitudinal mode respectively. The solid line is the double Gaussian fit mentioned in the text. The inset plots the extracted positions of the 'R' and 'L' peaks (down and up triangles) measured at 300 K, superimposed with previous time-of-flight HAS measurements of the Rayleigh mode and the longitudinal mode (circles and diamond markers) [35], and EELS measurements of the Rayleigh mode (square markers) [36].

angle of $\alpha = 144°$ was optimized for measuring this width. The 'R' peak is located close to a second much broader energy-loss peak, labelled 'L'.

In order to identify these two energy loss peaks, the spectra were fitted using a double Gaussian model and the position of the peaks was followed as a function of the scattering geometry. The inset plot in figure 8 shows the dispersion relation extracted for peak 'R' and peak 'L' (down and up triangles respectively) plotted on top of previous HAS measurements (circles and diamond markers) [35] and electron energy-loss spectroscopy (EELS) measurements (square markers) [36]. The 'R' peak clearly fits the previous measurements of the Rayleigh mode, extending the dispersion curve to the previously unmeasured low momentum transfer region. The lower peak intensity of the 'L' peak restricted the momentum transfer range where the position of the peak could be reliably determined; however, the extracted dispersion curve seems to be a continuation of the controversial 'Longtitudal mode' observed in previous higher momentum transfer measurements [35]. It is interesting to note that the real width of this mode (i.e. when optimizing the projected angle for the 'L' peak) is an order of magnitude wider then that of the Rayleigh mode. Finally, a smaller sharp peak can be seen above the noise level at the lower-energy end of the spectrum. This peak is a residual mirror peak of the Rayleigh mode, due to imperfect phase acquisition[3]. As we mentioned earlier, the method currently used to measure the imaginary polarization is an approximation which cannot completely eliminate artefact mirror peaks. It is important to note that when the spectrum is reconstructed without the imaginary component, the relative height of this artefact peak increases significantly by more than 400%, making the imaginary polarization measurement worthwhile.

After identifying the Rayleigh mode, we utilize the high resolution of the spectrum to perform a series of detailed measurements. The measured energy loss of the Rayleigh

---

[3] The mirror peaks which arise from a cosine transform or a non-perfect complex transform are symmetric with respect to the origin of the tilted wavelength spectrum. The position of the mirror peaks in the energy spectrum will vary depending on the tilted projection angle of the measurement.
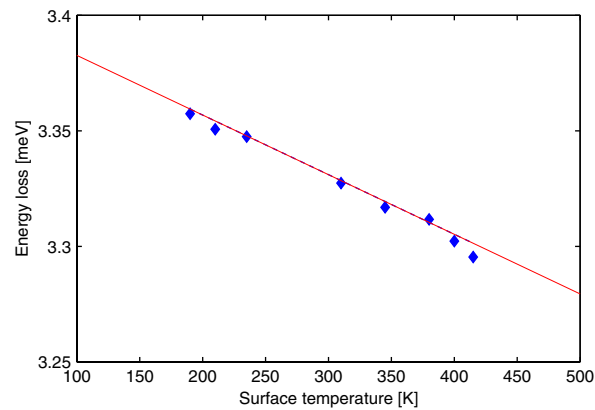
Figure 9. Energy loss of the Rayleigh mode as function of temperature. All the measurements were performed along the ⟨100⟩ crystal azimuth, $-5°$ off the specular direction. The line is a linear fit with a slope of -260 neV K^{-1}.

mode is plotted as a function of sample temperature in figure 9. The temperature-dependent measurements were all performed $-5°$ off specular, which corresponds to a momentum transfer of 0.27 Å^{-1} for the 3.3 meV energy loss of the Rayleigh mode. This momentum transfer value corresponds to $3\vec{M}/20$, where $\vec{M}$ is the Brillouin zone boundary.

The Rayleigh mode energy-loss peak undergoes a subtle decrease with increasing temperature. This softening of the mode with temperature is not surprising and has already been observed at higher momentum transfer values, corresponding to $\vec{M}/2$ [37]. The surprising feature seen from the ^{3}He spin-echo data is the small magnitude of the anharmonicity. Within the 225 K measurement range the total change is only 60 μeV, or using a linear fit the mode softens with a slope of 260 neV K^{-1}.

Comparing this slope with the measured behaviour at higher momentum transfer values [37], the slope is approximately an order of magnitude lower. Following the analysis of the time-of-flight measurements, we can also compare the anharmonicity of the T1 bulk mode with the Rayleigh mode behaviour. Surprisingly we see that at low momentum transfer values the surface mode appears to have a reduced anharmonicity with respect to the bulk. This result is surprisingly different from the enhanced anharmonicity observed at high momentum transfer values [37].

4.3. Quasi-elastic scattering: ultra-fast transport dynamics at surfaces

In a quasi-elastic helium atom scattering (QHAS) experiment [7, 8], which is a surface-sensitive analogue of quasi-elastic neutron scattering [38], the helium beam is used to probe aperiodic motion on the surface. The sensitivity of the experiment originates in a Fourier transform relation between the energy profile of the scattered beam and the Van Hove pair-correlation function [16]. The Van Hove pair-correlation function $G(\mathbf{r}, t)$ is a fundamental statistical tool which describes the dynamics; it can be interpreted classically as the probability of finding a particle at position $\mathbf{r}$, at a time t, given that a specific particle was at the origin at time $t = 0$ [16]. It is convenient to separate the pair correlation using the sum $G(\mathbf{r}, t) = G_\mathrm{s}(\mathbf{r}, t) + G_\mathrm{d}(\mathbf{r}, t)$ where the first and second terms are the self- and distinct-correlation functions. These two functions describe the probability of finding the same particle or different particles at the two positions respectively. While in general the functional form of the pair-correlation function is
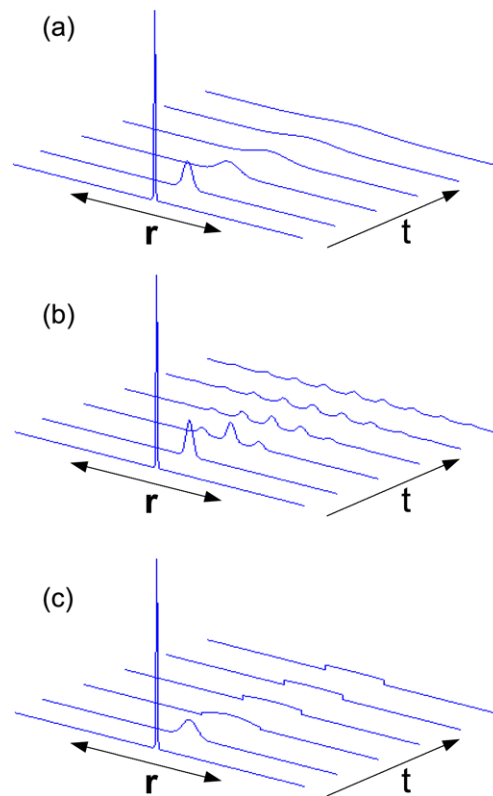
Figure 10. Illustration of the self-pair-correlation function. (a)–(c) illustrate the cases of continuous random motion, discrete jump diffusion and continuous random motion confined within a 1D rectangular well. In all three cases the function expands from a delta function at $t = 0$ due to the random motions. This expansion takes place continuously in (a) and (c) and through discrete sites in (b). The restricting geometry stops the expansion in (c) resulting in a steady-state displacement probability.

complex, when the motion is isolated (i.e. for low coverages and for weak interactions) the shape of the pair-correlation function is determined by the self-correlation term and is more easily visualized [39]. Figures 10(a)–(c) illustrate schematically the self-correlation function for some simple cases of 1D diffusion.

Figure 10(a) shows the case of normal Brownian diffusion. The definition of the self-correlation function dictates that at $t = 0$ the peak will be a delta function in **r**. As time evolves, random motion increases the displacement probability and the normalization condition of the probability density leads to a continuous drop in amplitude as the Gaussian envelope broadens. Figure 10(b) illustrates the case of jump diffusion. Here, we assume that the particle randomly hops between a discrete set of allowed sites. This scenario is typical for adsorbates which are located at specific lattice sites and spend a negligible amount of their time in the transition process in between the different sites. The resulting self-correlation function expands into a discrete set of allowed regions. As the time increases, more of these sites are occupied, leading to a broadening of the overall Gaussian envelope and a corresponding drop in amplitude, as was seen previously for the Brownian motion case. Finally, figure 10(c) illustrates the case of a particle which performs continuous random motion within a confining infinite square well. The initial dynamics are similar to those shown in figure 10(a); however, after a certain

characteristic time the particle has probed its confining geometry and eventually reaches a steady-state distribution within the region of confinement, indicating the loss of correlation between the initial and final locations.

The three examples above illustrate how the detailed shape of $G(\mathbf{r}, t)$ reflects the underlying microscopic mechanism of the dynamics. The method for measuring this function with a time-of-flight spectrometer has been described in detail both for neutron and for helium beams [16, 17], where it has been shown that, within the kinematic scattering approximation, the Fourier transform in time and in space of $G(\mathbf{r}, t)$ is the well known dynamic structure factor, $S(\Delta\mathbf{k}, \omega)$. The dynamic structure factor describes the probability of a scattering event with a momentum transfer and energy transfer of $\Delta\mathbf{p} = \hbar\Delta\mathbf{k}$ and $\Delta E = \hbar\omega$. The spectrum of a time-of-flight spectrometer measures the convolution of $S(\Delta\mathbf{k}, \omega)$ with the experimental energy resolution and momentum resolution functions.

The double Fourier transform relation between $G(\mathbf{r}, t)$ and $S(\Delta\mathbf{k}, \omega)$ enables us to study the microscopic diffusion mechanism by monitoring the functional form of $S(\Delta\mathbf{k}, \omega)$. The common feature of $S(\Delta\mathbf{k}, \omega)$ when the motion is aperiodic is a peak centered at the energy transfer origin ($\omega = 0$). Monitoring the width of this peak, known as the quasi-elastic broadening, as a function of $\Delta\mathbf{k}$ or surface temperature has been the method of choice in all the time-of-flight QHAS studies [7]. The $\Delta\mathbf{k}$ and temperature dependence of the peak width can be related to the underlying dynamics using several analytical models and numerical simulations [8, 40, 41]. Since the quasi-elastic broadening is typically much smaller than the experimental broadening, the dynamic structure factor needs to be deconvoluted from the time-of-flight spectrum. In order to perform this process reliably, a Lorentzian lineshape model for the dynamic structure factor was typically assumed when analysing time-of-flight data. We discuss the significance of this assumption later.

4.3.1. Interpreting the dynamics from a time-domain spin-echo measurement. From the graphical description of the wavelength intensity matrix presented earlier, we saw that the quasi-elastic peak forms a straight line at 45° to the positive horizontal axis. As was illustrated in the lower panel of figure 4, the optimal way of measuring the width of this feature is to use a $\alpha = 135°$ projection. In practice, such a projection is achieved by measuring the polarization while scanning the current magnitude and maintaining equal and opposite currents in the two coils, $I_1 = -I_2$ ($\kappa_1 = -\kappa_2$).

One method of analysing the underlying dynamics from the spin-echo measurement is to Fourier transform the measured polarization and convert the subsequent tilted wavelength spectrum into an energy transfer spectrum. A spectrum reconstructed in this way is equivalent to the dynamic structure factor. Thus, we could analyse the ultra-high resolution spin-echo data with the same analytical and numerical techniques used in the previous time-of-flight studies. However, as we describe in more detail below, an $\alpha = 135°$ polarization measurement is effectively performed in the time domain. In many cases, as will be illustrated later for both the CO/Cu(001) and the Na/Cu(001) systems, there is an advantage in analysing the spin-echo polarization scans directly in the time domain (i.e. without performing the Fourier transform).

The time domain is introduced using another experimental variable, which has the units of time, known as the spin-echo time. The spin-echo time is defined by the relation $t = \kappa m \langle\lambda_1\rangle^3 / h$, where $\kappa = \kappa_1 = -\kappa_2$ and $\langle\lambda_1\rangle$ is the mean wavelength of the incident beam. The justification for this variable transformation arises from the fact that the spin-echo time is a meaningful physical variable. The physical meaning of this variable becomes apparent when we consider an $\alpha = 135°$ spin-echo experiment quantum-mechanically.

Each helium atom which is successfully polarized in the first part of the instrument has a $+Y$ spin state, i.e. is polarized perpendicular to the beam-line and vertically in the

laboratory frame. The wavepacket describing an atom with a $+Y$ spin state can be written as a superposition of two wavepackets with spin states oriented along the positive and negative X axis respectively. When these two wavepackets enter the first precession field (also oriented along the positive X axis), they are accelerated and decelerated respectively, depending on their spin state. The two wavepackets travel through the precession field at different speeds, which can be calculated from energy conservation considerations [15]. Consequently, one of the wavepackets will arrive at the sample at a time, t, earlier then the other. For an $\alpha = 135°$ spin-echo measurement the second precession field is equal in magnitude but reversed in polarity. Thus the time and phase differences between the two wavepackets are exactly cancelled out by the inverse effect of the second precession field. When the surface studied is static, the two wavepackets interfere constructively at the end of the second field and recreate the helium wavefunction with its original $+Y$ spin orientation, leaving us with a fully polarized beam. However, if the surface changes during the time difference, t, between the scattering of the two wavepackets, then the different scattering processes lead to a residual phase difference which is not cancelled in the second precession coil. This difference in phase gives rise to destructive interference and a corresponding loss of beam polarization. Thus, scanning the final beam polarization as a function of the time difference between the wavepackets effectively monitors the dynamics taking place at different time intervals. Solving the spin dynamics quantum mechanically [15], it can been shown that this time difference is identical to the spin-echo time we defined earlier.

Within the kinematic scattering approximation, and assuming a quasi-elastic process (i.e. the energy transfer is smaller than the mean energy of the beam) the $\alpha = 135°$ spin-echo polarization, measured as function of time, is in effect an intermediate function between the pair-correlation function, $G(\mathbf{r}, t)$ and the dynamical structure factor, $S(\Delta \mathbf{k}, \omega)$ [9]. Thus within these approximations, the polarization can be written as being proportional to the spatial cosine Fourier transform of $G(\mathbf{r}, t)$,

$$P_Y(\Delta \mathbf{k}, t) \propto \int G(\mathbf{r}, t) \cos[2\pi(\Delta \mathbf{k} \cdot \mathbf{r})] \, d\mathbf{r}, \tag{4}$$

where $\Delta \mathbf{k} = (\Delta \mathbf{K}, \Delta k_z)$ is the 3D scattering wavevector related to the momentum transfer of the helium atoms and $\Delta \mathbf{K}$ denotes the component within the surface plane.

Within the spin-echo experiment, both the spin-echo time, t, and the momentum transfer parallel to the surface, $\Delta \mathbf{K}$, can be varied experimentally by changing either the current in the coils or rotating the sample respectively. Measuring the polarization for a sufficiently wide range of t and $\Delta \mathbf{K}$ values allows us to study the full dynamics contained in $G(\mathbf{r}, t)$.

4.3.2. Extending the experimental time range: measuring slower dynamics. The first diffusion system studied with the Cambridge spin-echo spectrometer was CO/Cu(001) [42]. The potential energy surface for this fundamental surface system had already been studied both experimentally and theoretically [43–45], yielding contradicting values for the underlying potential energy surface. Further numerical simulation work [46] has suggested that the observed QHAS broadenings, originally interpreted as related to the inter-cell jump diffusion, actually originated from the dephasing of the intra-cell vibration process.

Figure 11 is a surface plot which combines the spin-echo polarization curves measured for different ΔK values, along the $\langle 100 \rangle$ and $\langle 110 \rangle$ crystal azimuths. The first surprising observation is that the polarization decays remarkably slowly, reducing by less then 20% at $t = 0.4$ ns. The fact that the polarization does not decay significantly within the available spin-echo time range corresponds to a dynamic structure factor peak which is significantly narrower than the reconstruction resolution of the Cambridge apparatus, i.e. the diffusion of CO/Cu(001),
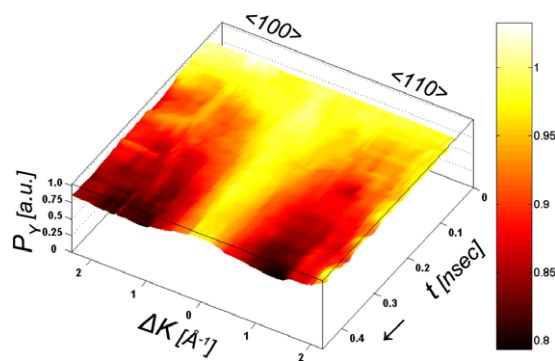
Figure 11. Helium spin-echo measurements of CO/Cu(001). The polarization is plotted as a function of the spin-echo time and the momentum transfer parallel to the surface. The measurements were performed at 190 K with a CO overpressure of 2×10^{-6} mbar, corresponding to a CO coverage of 0.1 ML. Measurements along the $\langle 110 \rangle$ and $\langle 100 \rangle$ crystal azimuths are shown to the right and to the left of the momentum transfer origin correspondingly. The surface plot presented was smoothed using a 2D sliding average to reduce the noise from individual polarization scans.

at a surface temperature of 190 K gives rise to sub-μeV QHAS broadenings. These extremely small QHAS broadenings explain why the inter-cell diffusion process was too slow to be measured with a time-of-flight apparatus. When studying a dynamic structure factor which is narrower then the reconstruction resolution of the instrument (≈ 3 μeV for the Cambridge apparatus), there is no benefit in Fourier transforming the polarization measurement. Under these conditions, the functional form of the quasi-elastic peak has to be assumed, and is similar to the requirement when studying sub-meV quasi-elastic peaks with a time-of-flight instrument. In this study the traditional Lorentzian lineshape assumption was made. Therefore, the time dependence of the measured polarization was fitted using a decaying exponent model.

A second observation which can be made from figure 11 is of the oscillatory ΔK dependence of the decay rate. This functional form is the Fourier transform of a discretely spaced $G(\mathbf{r}, t)$ (e.g. figure 4(b)), and is characteristic of a jump diffusion mechanism [47]. By comparing the measurements performed along $\langle 100 \rangle$ and $\langle 110 \rangle$ azimuths using both analytical analysis and molecular dynamics simulations, a potential energy surface and a friction term were extracted for the CO/Cu(001) system [42]. The extracted potential energy surface is characterized by an energy barrier of ≈ 125 meV for diffusion along both the bridge site and the four-fold hollow site directions. When comparing this experimental potential energy surface with more recent density-functional theory calculations [48], we see that the calculations seem to correctly predict the bridge barrier but significantly overestimate the hollow site barrier for diffusion. Thus, more work is still needed in order to reproduce the experimental potential energy surface of this basic surface system from first principles.

4.3.3. Studying surface diffusion: beyond the Lorentzian line shape assumption. An example which illustrates different insights from ultra-high resolution which apply to faster diffusing systems comes from recent measurements of the diffusion of sodium atoms on a Cu(001) surface [49]. The Na/Cu(001) system is particularly suitable for QHAS measurements as there are a wide range of accessible temperatures and the mobility of the sodium atoms is high. At low Na coverages the dynamics have been extensively and successfully studied using time-of-flight helium atom scattering [50–52]. The QHAS broadenings were extracted from the experimental time-of-flight data using a deconvolution procedure which assumes a
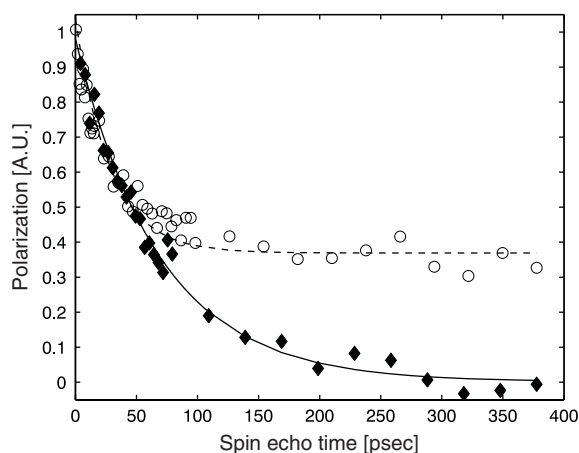
Figure 12. Spin-echo polarization curves of Na/Cu(001), measured at 155 K along the ⟨110⟩ crystal azimuth [49]. The diamonds markers show a normal polarization curve measured at $\Delta K = 0.6$ Å^{-1} and $\Theta = 0.04$ ML. The circle markers show an anomalous polarization curve measured at $\Delta K = 0.03$ Å^{-1} and $\Theta = 0.08$ ML.

single Lorentzian quasi-elastic peak. The temperature and momentum transfer dependences of the QHAS broadenings measured at low Na coverages were successfully reproduced by MD simulations, making it possible to reconstruct a potential energy surface for this system [51, 52]. On the other hand, for a higher sodium coverage, a discrepancy between the experimental results and MD simulations was encountered [53, 54], leaving the dynamics of the system at higher coverages unresolved.

The diamond markers plotted in figure 12 show a typical polarization curve measured with the helium spin-echo spectrometer using a low coverage of sodium on the surface (coverage, $\Theta = 0.04$ ML) [49]. At low coverages the polarization curves decay exponentially to zero. An exponential decay in time of the polarization corresponds to a Lorentzian-shaped quasi-elastic peak in the dynamic structure factor (due to the temporal Fourier transform relation) and is expected for a jump diffusion mechanism [47]. This observation retrospectively justifies the Lorentzian lineshape assumption made earlier for this specific case. Thus, it is not surprising that, when the decay rates of these polarization curves were analysed using MD simulations, the extracted potential energy surface parameters [49] were in good agreement with those derived previously from the data [51, 52].

An unexpected finding was observed when the sodium coverage was increased beyond 0.05 ML. At these higher coverages, a different kind of polarization curve was encountered. An example of such a curve is shown by the circular markers in figure 12. The functional form of the new curve, i.e. an initial decay which approaches constant non-zero polarization value at longer times, characterized curves measured at extremely low ΔK values (0.02 Å^{-1} < ΔK < 0.1 Å^{-1}) and coverages greater then $\Theta = 0.05$ ML. These curves are referred to as anomalous curves. The fact that the anomalous curves do not exponentially decay to zero corresponds to the dynamic structure factor having a non-Lorentzian peak shape.

In order to understand the shape of different polarization curves, we start by examining the relation between the time dependence of the polarization and the surface dynamics using equation (4). For simplicity, let us look at the first two examples of $G(\mathbf{r}, t)$ shown in figures 10(a) and (b). In both of these cases the width of $G(\mathbf{r}, t)$ increases continuously due to

21

the unrestricted nature of the random motion. The polarization, as given in equation (4), is a sum of cosine terms with a phase given by the dot product $\Delta\mathbf{k} \cdot \mathbf{r}$ and a relative weight factor given by $G(\mathbf{r}, t)$. As time increases, non-zero values of $\mathbf{r}$ have a non-zero weight; therefore, cosine terms with an increasing random phase are added to the sum. Eventually the sum is performed over a large enough random phase distribution that the sum (i.e. the polarization) reduces to zero.

The fact that the anomalous curves were seen at $|\Delta\mathbf{K}| \approx 0$ (i.e. at specular conditions) reveals the orientation of the observed motion. At specular conditions the scattering vector is oriented perpendicular to the surface ($\Delta\mathbf{k} = [0, 0, \Delta k_z]$). The dot product in equation (4) makes the parallel motion practically invisible to the experiment; thus at these scattering conditions it is only motions perpendicular to the surface plane which can randomize the phase and lead to a decay in polarization.

After identifying the orientation of the motion underlying the anomalous curves, we can readily understand why these curves decay to non-zero polarization (i.e. why the quasi-elastic energy peak is non-Lorentzian). The range of adsorbate motion perpendicular to the surface is inherently restricted, and governed by the potential well shape in the Z direction. Figure 10(c) illustrates $G(\mathbf{r}, t)$ for the case of 1D random motion in a restricted geometry (e.g. within perfectly reflecting walls). As was discussed earlier, in the restricted motion case, $G(\mathbf{r}, t)$ stops broadening, and converges to a steady-state configuration once the moving species has had sufficient time to probe the barriers. Equation (4) translates this phenomenon to a polarization which stops decaying. The residual steady-state polarization will depend on how randomized the phase is at the steady-state stage.

As a rule of thumb, if the product $\Delta k_z Z_{max} \gg 2\pi$ where Z_{max} denotes the maximum range of perpendicular motions, then the phase will be sufficiently randomized and the polarization will be equal to zero. When the polarization does not decay to zero we can use the residual polarization level to estimate the amplitude of the motion taking place. We can use a simple rectangular well model to estimate the effective range of motion underlying the anomalous curve shown in figure 12. Assuming a rectangular steady-state pair-correlation function and the Fourier transform relation in equation (4) results in a polarization which is a sinc function of the product $K_z Z_{max}$. Solving the Sinc for $\Delta k_z = 7$ Å^{-1} and a 40% decay of the polarization, we can estimate $Z_{max} \approx 0.2$ Å.[4]

The parallel and perpendicular motion taking place in the Na/Cu(001) system was studied by analysing both the normal and the anomalous curves as function of coverage and temperature [49]. The analysis indicates that below 0.05 ML the motion of the Na atoms is essentially 2D correlated motion, which is well described using a repulsive dipole interaction. Above 0.05 ML there is an onset of perpendicular motion. The conclusion from a MD fit to the full set of data is that the apparent height of the Na atoms varies according to the time dependent local coverage it experiences, due to the 2D random jump process [49]. Recent first-principles calculations suggest that the observed perpendicular motions are related to a significant redistribution of the electron charge density, which is triggered by the changes in the local coverage due to the underlying jump process [55].

Finally, it is important to note that the observation of non-Lorentzian peak shapes (non-exponential polarization decays) is not unique to this system. There are several other conditions which lead to deviations in the peak shape. For example, non-Lorentzian behaviour has been theoretically predicted both for low-friction systems and for highly correlated diffusion [56, 57]. In addition, a non-zero constant component of the polarization has already

---

[4] Since realistically the well will not be rectangular, the shape of the potential will lead to a smaller occupation of z values closer to the boundary; the value derived above should be treated as a lower-limit approximation for Z_{max}.

been observed in other spin-echo measurements performed at low-coverage adsorbate systems or with highly corrugated surfaces [5, 58]. In these cases, it is the underlying substrate or static defects on the surface which gives rise to a significant and occasionally dominant elastic contribution to the energy spectrum of the scattered beam.

5. Summary and outlook

In this review we have introduced the ^{3}He spin-echo technique, using a graphical description of the measurement process which allows elastic, inelastic and quasi-elastic measurements to be treated on an equal footing. We have illustrated the usefulness of this technique with a range of recent measurements covering these fields. It is self-evident that, in each of these cases, significant advances have been made through the application of the ^{3}He spin-echo technique to surfaces.

Today, surface science is often regarded as a mature field in which many of the interesting problems have already been resolved. However, science is often driven by the available instrumentation. For example, the fact that numerous surface structures have been resolved can be attributed to the wide availability of well established experimental techniques such as low-energy electron diffraction (LEED) or more recently scanning transmission microscopy (STM). From a dynamical point of view the situation is very different. For example, while several techniques can be used to measure macroscopic diffusion, the atomic-scale motion taking place on the surface typically lies well outside the experimentally available range. This lack of experimental data, combined with the significant limitations on the predictive capabilities of first-principles calculations, leave atomic-scale dynamics uncharacterized for most surface systems. Consequently, many active surface research areas, such as molecular-beam epitaxy (MBE) growth, heterogeneous catalysis or self-assembled nanostructures, all include an unknown dynamical element. The application of time-of-flight helium scattering to study surface dynamics, combined with the significant advances recently made possible with ^{3}He spin-echo, enable new experimental studies of a wide range of surface dynamics systems, contributing significantly to our understanding in these research areas.

One of our immediate focuses is on the development of further potential energy landscapes. While surface structure measurements have been an extremely useful benchmark for the development of theory, the potential energy surfaces which govern the surface dynamics provide a much more stringent test of any theoretical calculation. Experimental potential energy surfaces for complex surface systems, where state of the art theory regularly breaks down, can be used to illuminate the strength and weaknesses of various theoretical approaches, stimulating further theoretical development.

Another promising research activity, which reaches beyond understanding the dynamics of a specific surface system, is studying the atomic-scale interactions and the frictional forces which govern the motion of an atom or a molecule. The pair-correlation functions which are measured in a helium-scattering experiment yield the atomic-scale mechanism of the dynamics, not just the total mobility rate. Thus, physical properties such as lateral adsorbate interactions and atomic-scale frictional coupling, which play a critical role in a wide range of diverse fields, can be extracted from the experimental data.

QHAS, and indeed HAS in general, has typically been applied to relatively simple surface systems. Whilst it remains important to acknowledge that, with a reciprocal space technique, systems need to be at least moderately well defined, our longer-term aims include applying spin-echo to progressively more complex systems, including larger molecules and nanostructured substrates. Consequently, molecular modes and confinement effects are likely to become progressively more important in the dynamics. Such work will benefit from two

complementarities with other techniques. First STM, which operates in real space at the other end of the time spectrum (very slow times in the case of STM, compared with very fast times for spin-echo), which will help understand the real-space detail of systems. Second, quasi-elastic neutron scattering provides a bulk analogue of the same experiment. The combination of the two opens the potential for exploring systems with both bulk and surface transport components (e.g. diffusion in 3D matrices, such as zeolites).

In terms of the instrumentation, the key to wide application of the technique is to maximize the signal available. Given that typical helium detector efficiencies are 10^{-4}–10^{-5}, there is considerable scope for improvement, particularly given that high temporal resolution is not required. There is also considerable scope for increasing the instrument resolution by using stronger precession fields. Increasing the resolution will further increase the applicability of the technique to slower-moving systems and will allow us to study more complex surface systems, where the lineshape analysis plays an important role.

Overall, the recent experimental studies performed with the spin-echo technique have barely touched on what we anticipate will be an important new field. We believe the wealth of the data which awaits will more than justify the effort of building new ^{3}He spin-echo instruments, to maintain worldwide progress in this emerging field of atomic-scale surface dynamics.

Acknowledgments

Appendix. The energy resolution of the reconstructed spectra

The Fourier transform relation between the polarization and the projected wavelength spectrum defines the elementary resolution condition in wavelength space. Using the resolution condition for a discrete Fourier transform, the minimal interval in wavelength space, $\Delta\lambda$, will be related to the maximal value of $\kappa = \sqrt{\kappa_1^2 + \kappa_2^2}$ by the relation $\Delta\lambda = 0.5(\kappa_{\max})^{-1}$. Thus the ultimate resolution in wavelength space is restricted by the maximal value of the precession field we can apply. When we convert the wavelength spectrum to the more traditional scattered-energy spectrum, we need to also include the nonlinear relation between the wavelength and energy ($\Delta E = -\Delta\lambda h^2/m\lambda^3$); therefore the energy resolution improves significantly for lower scattered energies. For example, using a 8 meV beam, the Cambridge apparatus can reconstruct the quasi-elastic peak with $\Delta E \approx 3\ \mu$eV. The criteria discussed above dictate the resolution to which a quasi-elastic spectrum can be reconstructed without making any lineshape assumption. When a certain lineshape can be assumed, a quasi-elastic broadening as small as 50 neV can be detected with the same apparatus [42]. The consequences of lineshape assumptions are discussed in section 4.3.3.

When reconstructing inelastic spectra there are two additional mechanisms which need to be considered and are typically the dominant limitation on the experimental energy resolution; curvature broadening and angular broadening. *The curvature broadening* mechanism arises from the projection operation discussed earlier. An optimal projection will only conserve the real width of a 2D feature if it follows a straight line in the λ_1, λ_2 space. The nonlinear relation between energies and wavelengths results in the fact that a fixed energy-loss or energy-gain

process defines a high-intensity curve (rather than a high-intensity line) in the wavelength space. The degree of curvature, and the resulting broadening in the projection, is a function of both the energy loss/gain and the dispersion relation of the excitation, $\Delta E(\Delta \mathbf{K})$. Since the approximation of a curve to a line improves for shorter curves, the more monochromatic the beam is, the smaller the curvature broadening effect is.

The angular broadening mechanism only applies when the excitation studied is dispersive (i.e. $\mathrm{d}\Delta E/\mathrm{d}\Delta K \neq 0$). The finite angular resolution of the instrument means that atoms with identical incoming wavelength can scatter with slightly different scattering geometries and correspondingly slightly different values of $\Delta \mathbf{K}$. The dispersion relation will translate this to a difference in the scattered wavelength (energy); therefore each value of λ_1 will in practice correspond to a certain range of λ_2 values. The width of that range is a function of the dispersion relation of the specific excitation studied and the angular resolution of the machine ($\approx 0.1°$ for the Cambridge apparatus).

The contribution from both of these effects needs to be calculated specifically for each measurement, especially when analysing subtle features such as the real width of an excitation. Calculations performed for low-energy surface phonons using the current angular and velocity spread of the Cambridge apparatus result in instrumental energy broadenings which are typically a few tens of μeV wide [5], approximately one order of magnitude larger than the instrumental energy resolution for reconstructing the quasi-elastic spectrum.

The angular broadening effect which is typically the dominant contributor can be minimized by either reducing the angular resolution of the apparatus, tilting the solenoid coils [59] or adding corrector coils [5]. Applying any one of these changes should significantly reduce the current gap between the experimental resolution of quasi-elastic and inelastic scattering measurements.

References

[1] Barth J V 2000 *Surf. Sci. Rep.* **40** 75–149
[2] Miller D R 1988 vol 1 (Oxford: Oxford University Press) chapter 2, pp 14–53
[3] Toennies J P and Winkelmann K 1977 *J. Chem. Phys.* **66** 3965–79
[4] Hofmann F and Toennies J P 1996 *Chem. Rev.* **96** 1307–26
[5] Alexandrowicz G 2005 Helium spin echo spectroscopy: measuring the dynamics of atoms, molecules and surfaces *PhD Thesis* University of Cambridge
[6] Farias D and Rieder K H 1998 *Rep. Prog. Phys.* **61** 1575–664
[7] Graham A P 2003 *Surf. Sci. Rep.* **49** 115–68
[8] Jardine A P, Ellis J and Allison W 2002 *J. Phys.: Condens. Matter* **14** 6173–91
[9] Mezei F 1980 *Neutron Spin Echo* (*Springer Lecture Notes in Physics*) (Berlin: Springer)
[10] Dekiviet M, Dubbers D, Shmidt C, Scholz D and Spinola U 1995 *Phys. Rev. Lett.* **75** 1919–22
[11] Druzhinna V and DeKieviet M 2003 *Phys. Rev. Lett.* **91** 193202
[12] Jardine A P, Fouquet P, Ellis J and Allison W 2001 *Rev. Sci. Instrum.* **72** 3834–41
[13] Dworski S, Alexandrowicz G, Fouquet P, Jardine A P, Allison W and Ellis J 2004 *Rev. Sci. Instrum.* **75** 1963
[14] Fouquet P, Jardine A P, Dworski S, Alexandrowicz G, Allison W and Ellis J 2005 *Rev. Sci. Instrum.* **76** 053109
[15] Gahler R *et al* 1999 *Physica* B **229** 1
[16] Van Hove L 1954 *Phys. Rev.* **95** 249–62
[17] Levi A C, Spadacini R and Tommei G E 1982 *Surf. Sci.* **121** 504–18
[18] Jardine A P, Dworski S, Fouqet P, Alexandrowicz G, Riley D J, Lee G Y H, Ellis J and Allison W 2004 *Science* **304** 1790
[19] Riley D J, Jardine A P, Dworski S, Alexandrowicz G, Fouquet P, Ellis J and Allison W 2007 *J. Chem. Phys.* at press
[20] Riley D J, Jardine A P, Alexandrowicz G, Ellis J and Allison W 2007 in preparation
[21] Riley D J 2005 Atom surface potentials from measurements of selective adsorption resonances *PhD Thesis* University of Cambridge
[22] Frisch R and Stern O 1933 *Z. Phys.* **84** 430–42

[23] Estermann I and Stern O 1930 *Z. Phys.* **61** 95–125
[24] Hoinkes H and Wilsch H 1992 *Helium Atom Scattering from Surfaces* ed E Hulpke (Berlin: Springer) chapter 6
[25] Chow H and Thompson E D 1976 *Surf. Sci.* **59** 225–51
[26] Vargas M C and Mochán W L 1996 *Surf. Sci.* **355** 115–26
[27] Celli V, Eichenauer D, Kaufhold A and Toennies J P 1985 *J. Chem. Phys.* **83** 2504–2520
[28] Fowler P W and Hutson J M 1986 *Phys. Rev.* B **33** 3724–35
[29] Eichenauer D and Toennies J P 1988 *Surf. Sci.* **197** 267–76
[30] Ellis J, Hermann K, Hoffman F and Toennies J P 1995 *Phys. Rev. Lett.* **75** 886–9
[31] Ellis J, Toennies J P and Witte G 1995 *J. Chem. Phys.* **102** 5059–70
[32] Graham A, Hofmann F and Toennies J P 1996 *J. Chem. Phys.* **104** 5311–6
[33] Bracco G, Bruschi L, Tatarek R, Franchini A and Bortolani V 1996 *Europhys. Lett.* **34** 687
[34] Gester M, Kleinhesselink D, Ruggerone P and Toennies J P 1994 *Phys. Rev.* B **49** 5777
[35] Benedek G, Ellis J, Luo N S, Reichmuth A, Ruggerone P and Toennies J P 1993 *Phys. Rev.* B **48** 4917
[36] Wuttig M, Franchy R and Ibach H 1986 *Z. Phys.* B **65** 71
[37] Benedek G and Toennies J P 1992 *Phys. Rev.* B **46** 13643
[38] Bee M 1988 *Quasielastic Neutron Scattering* (Bristol: Institute of Physics Publishing)
[39] Vineyard G H 1958 *Phys. Rev.* **110** 999–1010
[40] Ellis J and Toennies J P 1994 *Surf. Sci.* **317** 99–108
[41] Ellis J and Graham A P 1997 *Surf. Sci.* **377–379** 833–42
[42] Alexandrowicz G, Jardine A P, Fouquet P, Dworski S, Allison W and Ellis J 2004 *Phys. Rev. Lett.* **93** 156103
[43] Graham A P, Hofmann F, Toennies J P, Williams G P, Hirschmugl C J and Ellis J 1998 *J. Chem. Phys.* **108** 7825–34
[44] Graham A P and Toennies J P 2001 *J. Chem. Phys.* **114** 1051–2
[45] Ge Q and King D A 2001 *J. Chem. Phys.* **114** 1053–4
[46] Jardine A P, Ellis J and Allison W 2004 *J. Chem. Phys.* **120** 8724
[47] Chudley C T and Elliot R J 1961 *Proc. Phys. Soc. Lond.* **77** 353–61
[48] Fouquet P, Olsen R A and Barends E J 2003 *J. Chem. Phys.* **119** 509–14
[49] Alexandrowicz G, Jardine A P, Allison W and Ellis J 2006 *Phys. Rev. Lett.* **97** 156103
[50] Ellis J and Toennies J P 1993 *Phys. Rev. Lett.* **70** 2118–21
[51] Graham A P, Hofmann F, Toennies J P, Chen L Y and Ying S C 1997 *Phys. Rev. Lett.* **78** 3900–3
[52] Graham A P, Hofmann F, Toennies J P, Chen L Y and Ying S C 1997 *Phys. Rev.* B **56** 10567–78
[53] Ellis J, Graham A P, Hofmann F and Toennies J P 2001 *Phys. Rev.* B **63** 195408
[54] Cucchetti A and Ying S C 1999 *Phys. Rev.* B **60** 11110
[55] Fratesi G *et al* 2007 in preparation
[56] Vega J L, Guantes R and Miret-Artès S 2004 *J. Phys.: Condens. Matter* **16** S2879
[57] Serra A and Ferrando R 2002 *Surf. Sci.* **515** 588
[58] Hedgeland H *et al* 2007 in preparation
[59] Mezei F 1978 *Neutron Inelastic Scattering* (Vienna: IAEA) p 125